Fractal defect states in the Hofstadter butterfly

Yoshiyuki Matsuki, Kazuki Ikeda, and Mikito Koshino

Phys. Rev. B **104**, 035305 — Published 26 July 2021

DOI: 10.1103/PhysRevB.104.035305

Fractal defect states in the Hofstadter butterfly

Yoshiyuki Matsuki,* Kazuki Ikeda,† and Mikito Koshino‡
Department of Physics, Osaka University, Toyonaka, Osaka 560-0043, Japan

We investigate the electronic properties in the Bloch electron on a two-dimensional lattice with vacancies in the uniform magnetic field. We show that a single vacancy site introduced to the system creates a defect energy level in every single innumerable fractal energy gap in the Hofstadter butterfly. The wavefunctions of different defect levels have all different localization lengths depending on their fractal generations, and they can be described by a single universal function after an appropriate fractal scaling. We also show that each defect state has its own characteristic orbital magnetic moment, which is exactly correlated to the gradient of the energy level in the Hofstadter diagram. Probing the spatial nature of the defect-localized states provides a powerful way to elucidate the fractal nature of the Hofstadter butterfly.

I. INTRODUCTION

The Hofstadter butterfly is the energy spectrum of Bloch electrons moving in a two-dimensional lattice under a uniform magnetic field, which is characterized by a nested fractal band structure [1–7]. It has been actively studied in condensed matter physics [8–15] and non-equilibrium dynamics [16–22], and also from a wide variety of perspectives including mathematics [23–29] and quantum geometry [30, 31]. Experimentally, the evidence of the fractal nature of the Hofstadter spectrum was found in various systems, such as GaAs/AlGaAs heterostructures with superlattices [32–34], ultracold atoms in optical lattices [35–37], graphene-based moiré superlattices [38–40], photons with the superconducting qubits [41] and one-dimensional acoustic array [42–44].

Currently, however, the experimental observations of the butterfly are mostly limited to the measurement of the spectral structure and the transport properties. Actually, richer fractal information is encoded in the wavefunctions of the Hofstadter butterfly, but it is generally considered to be difficult to access in experiments. The characteristic spatial property of each wavefunction is generally averaged out in the physical observables due to the summation over the Bloch momentum.

In this paper, we theoretically propose that the spatial structure in the Hofstadter system can be elucidated by introducing a point defect to the system. In an electron system under a magnetic field, generally, a point disorder potential gives rise to defect localized states in the energy gaps between Landau levels [45–51]. The effects of lattice defects on the Hofstadter spectrum were investigated in some past works [52–59], and the in-gap defect levels were found at a certain magnetic flux [59]. However, it has not been clear how the self-similar nature is manifested in the defect localized states.

In this article, we study the Hofstadter problem with vacancy defects in a square lattice to investigate the fractal properties of defect states. We show that a single vacancy site introduced to the system creates a defect energy level in every single innumerable fractal energy gap in the Hofstadter butterfly. We find that the wavefunctions of different defect levels have all different localization lengths depending on their fractal generations, and importantly, the localization length of any levels can be approximately described by a single universal curve after an appropriate fractal scaling. We also find that the defect states are accompanied by an orbital magnetic moment due to rotating electric current, and its magnitude exactly coincides with the gradient of the energy gap in the Hofstadter diagram. These results give a new quantitative perspective on the spatial fractal nature of the Hofstadter butterfly, and provide a powerful way to elucidate the fractal nature of the Hofstadter butterfly by probing the defect states.

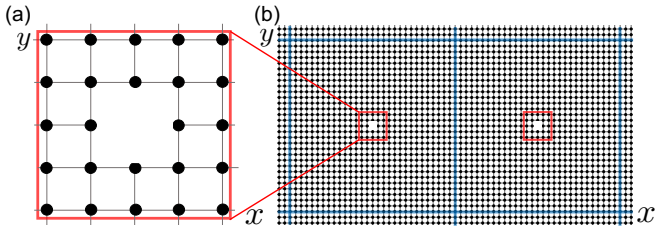

FIG. 1. (a) Square lattice with a single point vacancy and (b) its periodic superlattice with 30×30 supercell

II. FORMULATION

We consider a square lattice with a single-site defect as illustrated in Fig. 1. We assume that the system is periodic with $N \times N$ supercell and each supercell includes a single vacancy site. The system is under a uniform magnetic field B perpendicular to the system. Let $\phi = Ba^2/(h/e)$ be the number of magnetic flux quanta per a 1×1 plaquette, where $a = 1$ is the spacing between the lattice points. In what follows, we consider a single

* ymatsuki@het.phys.sci.osaka-u.ac.jp
† kikeda@het.phys.sci.osaka-u.ac.jp
‡ koshino@phys.sci.osaka-u.ac.jp

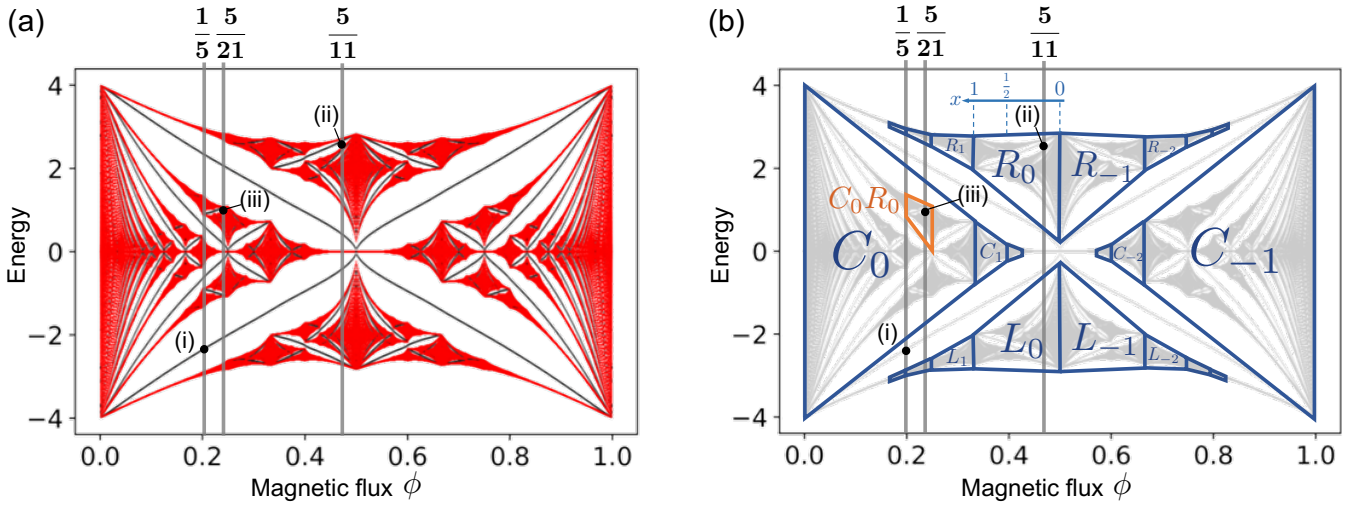

FIG. 2. (a) Energy spectrum of 30×30 superlattice with a single-site defect, which is plotted against the magnetic flux ϕ.The red and black dots represent the bulks states and the defect-localized states, respectively. The labels (i), (ii) and (iii) correspond to the wavefunctions shown in Fig. 3. (b) Subcell decomposition of the Hofstadter butterfly (see the text). The states (i), (ii) and (iii) belong to the positive gradient principal gaps of the main spectrum, R_0 and C_0R_0, respectively.

orbital tight-binding Hamiltonian,

$$H = -t \sum_{\substack{\langle m,n\rangle \\ m,n\neq d}} \mathrm{e}^{i\theta_{mn}} c_m^\dagger c_n, \tag{1}$$

where $t\,(>0)$ is the hopping parameter, $\langle m,n\rangle$ is a pair of the nearest neighbor sites, $c_n^\dagger(c_n)$ is the creation (annihilation) operator at site n, d is the site of defects, $\theta_{mn} = -(e/\hbar)\int_n^m \boldsymbol{A}\cdot d\boldsymbol{\ell}$ is the Peierls phase [60], and $\boldsymbol{A} = (0, Bx, 0)$ is the vector potential. We take $t = 1$ throughout this letter. In a perfect lattice without a defect under a rational magnetic flux $\phi = p/q$ (p, q: coprime integers), the energy band splits into q subbands [5].

The number of total magnetic fluxes penetrating an entire supercell is $\Phi = N^2\phi$. For $\Phi = P/Q$ with coprime integers P and Q, the eigenstates of the system can be taken as magnetic Bloch states, which satisfy the following conditions [3, 61, 62]:

$$\psi(\boldsymbol{r}+\boldsymbol{L}_1) = e^{ik_xL_1}e^{-i2\pi eBL_1y}\psi(\boldsymbol{r}), \tag{2}$$
$$\psi(\boldsymbol{r}+\boldsymbol{L}_2) = e^{ik_yL_2}\psi(\boldsymbol{r}), \tag{3}$$

where $\boldsymbol{L}_1 = (QNa, 0)$ and $\boldsymbol{L}_2 = (0, Na)$ are the primitive lattice vectors of the magnetic unit cell. Then the eigen-energies and eigen-wavefunctions can be obtained by diagonalizing $QN^2 \times QN^2$ Hamiltonian matrix. We also perform similar calculations and analyses for a honeycomb lattice with periodic vacancies, which are presented in Appendix A.

III. FRACTAL DEFECT STATES

A. Energy spectrum and wavefunctions

Fig. 2(a) shows the energy spectrum of 30×30 superlattice with a single-site defect, plotted against the magnetic flux ϕ. The red and black dots represent the bulk states and the defect-localized states, respectively. Here the defect-localized states are identified by the condition that the wave amplitude within seven-site distance from the defect point is more than 60% of the total amplitude. By this condition, we can detect most of the localized states except for ones with very large localization lengths appearing in a close vicinity of $x = 0$ and 1. The complete classification of the localized/extended states requires the calculation with infinite superlattice period. In Fig. 2(a), we observe that a defect level exists in every single gap, indicating that the spectrum of the defect states inherits the nested fractal structure of the Hofstadter butterfly. It was pointed out that the similar impurity states appear in all the energy gaps in 1D Harper's model with a single point impurity [63–65], which corresponds to a 1D line defect in the 2D lattice under magnetic field. Here we consider a 0-dimensional point defect in the 2D lattice.

The left panels in Fig. 3 represent the squared wavefunctions of defect levels (i), (ii) and (iii) in Fig. 2, which are taken from different minigaps of the Hofstadter butterfly. Note that the structure of the defect-state wavefunctions converges when the superperiod is much greater than the localization length. Here the eigenstates are calculated in 40×40 superlattice, which is sufficiently large for the defect states argued in this paper. We clearly observe that the defect-state wavefunctions all localize around the vacancy, while their characteristic

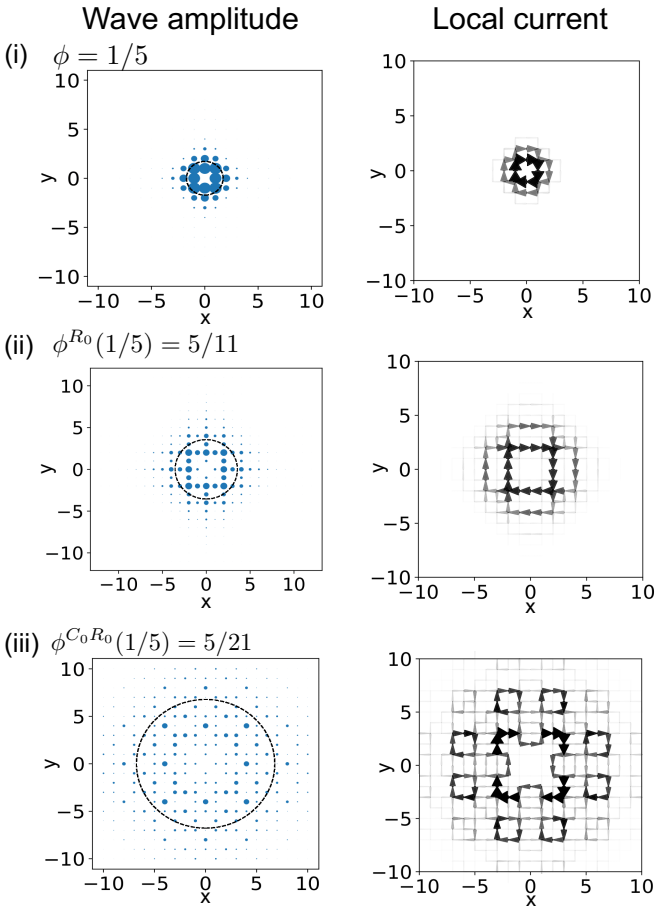

FIG. 3. Distribution of the wave amplitude (left) and the local electric current (right) of the defect states (i), (ii) and (iii), which are indicated in Fig. 2. The dots size in the left figures represents the magnitude of wavefunction, and thickness and color depth of the arrows in the right figures represent the local current amplitude.

length scales are completely different. Actually, as shown in the following, the localization length of the defect states is a good quantitative indicator of the fractal generation of the minigap.

B. Fractal scaling rule

To demonstrate this, we first introduce an addressing rule for the fractal structure [5, 66–69]. As shown in Fig. 2(b), the whole energy spectrum in $0 \le \phi \le 1$ (referred to as the main spectrum in the following) can be divided into left, right, center subcells, which are labelled by L_n, R_n and C_n ($n \in \mathbb{Z}$), respectively. Due to the fractal nature of the Hofstadter butterfly, each subcell has the same gap structure as that of the whole spectrum. We can define the local variable x for each subcell which works as an effective magnetic flux [5, 66]. Specifically, the gap structure of a subcell plotted against the local variable $x\,(0 \le x \le 1)$ is identical to that of the main spectrum plotted against the magnetic flux $\phi\,(0 \le \phi \le 1)$. As we will see, the local variable x is an essential parameter to compare the localization lengths of different subcells. The global variable ϕ and the local variable x for the subcell $X_n\,(X = L, R, C)$ are related by $\phi = \phi^{X_n}(x)$, where

$$\phi^{L_n}(x) = \phi^{R_n}(x) = (n + x + 2)^{-1}, \tag{4}$$

$$\phi^{C_n}(x) = [2 + 1/(n + x)]^{-1}. \tag{5}$$

In Fig. 2(b), we present an axis of the local variable x for R_0 subcell, where $x = 0, 1/2, 1$ correspond to $\phi = 1/2, 2/5, 1/3$, respectively. The main spectrum can also be regarded as a single subcell, where the local variable is the magnetic flux itself, i.e., $\phi = x$.

By repeating this addressing scheme, we can define the subcells in higher generations. For instance, X_mY_n refers to subcell Y_n in subcell X_m in the main spectrum. The relation between the local variable x for subcell X_mY_n and the global variable ϕ is given by $\phi = \phi^{X_m}(\phi^{Y_n}(x))(\equiv \phi^{X_mY_n}(x))$.

For each subcell, we define the positive (negative) principal gap as the diagonal gap running from the lower (upper) left corner to the upper (lower) right corner of the subcell plotted against ϕ. Any gap in the Hofstadter diagram can be uniquely identified as the positive or negative principal gap of a specific subcell or of the main spectrum.

In the following, we compare the localization lengths of the corresponding defect states in the principal gaps of different subcells, which share the same local variable x. The defect levels (i), (ii) and (iii) in Figs. 2 and 3 are actually taken from the positive principal gaps of the main spectrum, R_0 and C_0R_0, respectively, with the same local variable $x = 1/5$. The global variables ϕ for (i), (ii) and (iii) are $1/5$, $\phi^{R_0}(1/5) = 5/11$ and $\phi^{C_0}(\phi^{R_0}(1/5)) = 5/21$, respectively. For each state, we define the localization length ξ by $\xi^2 = \sum_i |\mathbf{r}_i - \mathbf{r}_0|^2 |\psi(\mathbf{r}_i)|^2$, where $\psi(\mathbf{r}_i)$ is the wave amplitude at site $\mathbf{r}_i$, and $\mathbf{r}_0$ is the vacancy position. Here we show that the ratio of ξ's of different subcells is approximately equal to the ratio of the denominators of ϕ of those states. For the states (i), (ii) and (iii) in Fig. 3, for instance, this claims that the ratio of the ξ's of the three states is $5 : 11 : 21$. Indeed, it approximates the ratio of the numerically calculated values $\xi = 1.716, 3.547, 6.774$, respectively (indicated by radii of circles in Fig. 3). The reason for this scaling rule can be understood by considering an ideal system without defects. Specifically, the Schrödinger equation for the ideal square lattice with $\phi = p/q$ is reduced to a one-dimensional Harper's equation with the spatial period of q [2, 5]. The period q works as the reference length scale to compare the wavefunctions in different fractal levels; for example, an eigenstate of Harper's equation at $\phi = 1/5$ and the corresponding state of R_0 cell at $\phi = \phi^{R_0}(1/5) = 5/11$ have similar structures with length scales of $5 : 11$. Naturally, the defect states take over the same scaling feature.

Let $\xi(\phi)$ be the localization length of the defect state in the principal gap of the main spectrum at the flux ϕ, and $\xi^{X_n}(x)$ be that of subcell X_n at local variable x. According to the argument above, we have the relation $\xi(p/q)/q = \xi^{X_n}(p/q)/D[\phi^{X_n}(p/q)]$, where $D[\phi]$ is the denominator of ϕ. Using Eqs. (4) and (5), this immediately leads to the relation between ξ and ξ^{X_n},

$$\xi(x) = \phi^{R_n}(x)\xi^{R_n}(x) = \phi^{L_n}(x)\xi^{L_n}(x), \tag{6}$$

$$\xi(x) = \frac{\phi^{C_n}(x)}{n+x}\xi^{C_n}(x), \tag{7}$$

which is a key finding of this work. Note that, although the denominator $D[x]$ is not a continuous function of x, the scaling ratio $\xi^{X_n}(x)/\xi(x)$ is a continuous function of x. Similarly, the relation for higher fractal generations can be obtained from $\xi(p/q)/q = \xi^{X_mY_n\cdots}(p/q)/D[\phi^{X_mY_n\cdots}(p/q)]$. For C_0R_0 subcell, for instance, it gives $\xi(x) = \phi^{C_0R_0}(x)\xi^{C_0R_0}(x)$.

In Fig. 4 , we plot (a) the localization lengths $(\xi, \xi^{R_0}, \xi^{R_1}, \xi^{C_0R_0})$ and (b) the renormalized values $(\xi, \phi^{R_0}\xi^{R_0}, \phi^{R_1}\xi^{R_1}, \phi^{C_0R_0}\xi^{C_0R_0})$ as functions of the local variable x. Here the solid and dashed curves represent the positive and negative principal gaps, respectively. The two curves are identical for the main spectrum due to the electron-hole symmetry. We see that the renormalized localization lengths [Fig. 4(b)] quantitatively match in a wide range of x. The $\xi(x)$ diverges at $x = 0$ in proportion to $1/\sqrt{x}$, corresponding to the fact that the length scale in a weak magnetic field is given by the magnetic length $\sqrt{\hbar/(eB)}$. We have the same feature in $x = 1$ symmetrically. At $x = 1/2$, we notice that the $\xi(x)$ diverges only in the negative gaps of the subcells, while it remains finite in the positive gaps. This links to the fact that the negative gaps close while the positive gaps are open at $x = 1/2$. For the main spectrum and any subcells centered at $E = 0$, the positive and negative gaps both close at $x = 1/2$ at the same time because of the electron-hole symmetry, and the localization lengths both diverge accordingly.

In Fig. 4, we also notice side peaks to the left and right from $x = 1/2$. The localization length of defect states generically tends to be larger when the corresponding energy gap width is smaller, and the side peaks actually correspond to $x = 1/3$ and $2/3$ where the size of the energy gap locally shrinks. This is the most prominently seen in the negative principal gap of R_0 subcell.

C. Exceptional scaling rules

In the previous subsection, we demonstrated that the localization length of defect state in each minigap of the Hofstadter butterfly is approximately described by a single universal function when it is appropriately scaled. However, there are some exceptional gaps in the spectrum, where the localization lengths follow different scaling curves. An exceptional scaling behavior occurs in the principal gaps of any subcells ending with C_0, i.e.,

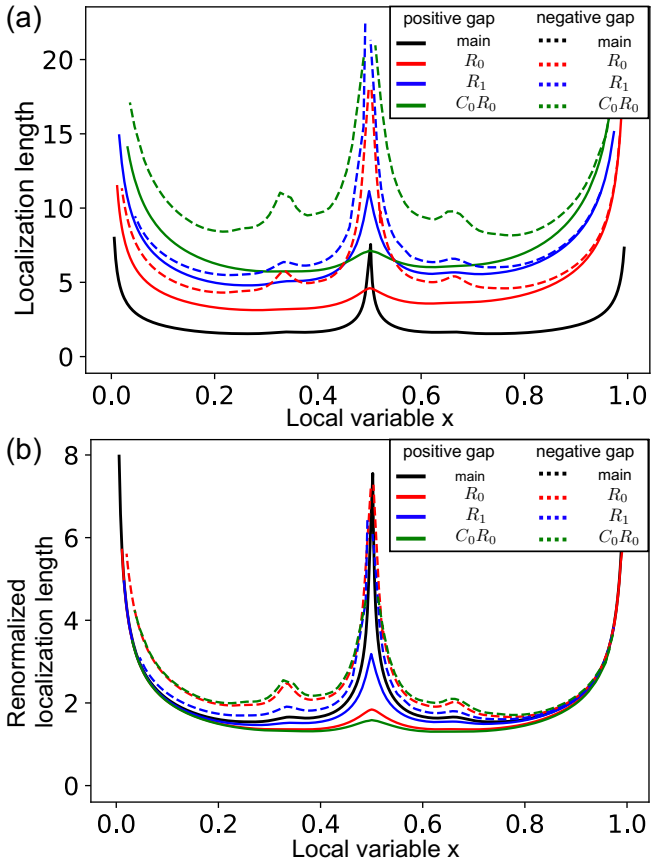

FIG. 4. (a) Localization lengths of different subcells, $\xi, \xi^{R_0}, \xi^{R_1}, \xi^{C_0R_0}$, and (b) their renormalized values $\xi, \phi^{R_0}\xi^{R_0}, \phi^{R_1}\xi^{R_1}, \phi^{C_0R_0}\xi^{C_0R_0}$ as functions of the local variable x.

$XY\cdots C_0$. Fig. 5(a) shows the renormalized localization lengths [Eqs. (6) and (7)] of the positive principal gaps of the main cell, C_0, C_0C_0 and $C_0C_0C_0$ subcells $[\xi, (\phi^{C_0}/x)\xi^{C_0}, (\phi^{C_0C_0}/x)\xi^{C_0C_0}, (\phi^{C_0C_0C_0}/x)\xi^{C_0C_0C_0}]$ as functions of the local variable x. Here $(C_0)^n$ subcell is a region sandwiched by $(n-1)$-th electron/hole Landau gaps in the weak field limit, and spreads in the magnetic flux range $0 \le \phi \le 1/(2n+1)$ [Eq. (5)]. We observe that the curves slightly shift in relative to each other in the limit of $x \to 0$, whereas they precisely match in $x \gtrsim 1/2$.

The reason for the deviation can be understood as follows. In the weak magnetic field limit, the principal gaps of C_0, C_0C_0 and $C_0C_0C_0$ subcells correspond to the second, third and fourth lowest gaps of the Landau-level spectrum, respectively [Fig. 5(c)]. This is in contrast to any subcells NOT ending with C_0, where the principal gap definitely connects to the lowest gap (the gap just above the lowest Landau level) in the magnetic Bloch subband at $x = 0$. The characteristic length scale of the n-th Landau level wavefunction φ_n is given by $\sqrt{n+1/2}\,l_B$, where $l_B = \sqrt{\hbar/(eB)}$ is the magnetic length. Accordingly, the defect-localized state which exists between the Landau levels $n-1$ and n should have the length scale of the order of $\sim \sqrt{n}\,l_B$, and the depen-

dence on n results in the different scaling curves. Indeed, the localization lengths of the main cell, C_0, C_0C_0,and $C_0C_0C_0$ subcells at a small magnetic field ($x = 11/9800$) are very well fitted by

$$\xi \approx 2\sqrt{n - 0.37}\, l_B, \tag{8}$$

with $n = 1, 2, 3$ and 4, respectively, where $l_B = a/\sqrt{2\pi x}$. In Appendix B, we show that the numerical result (8) qualitatively agrees the analytical expression for a continuum 2D electron with a delta-function impurity.

Similarly, the same scaling rule is applicable to $XY\cdots Z(C_0)^n$ subcells. In Fig. 5(b), we plot the renormalized localization lengths of the principal gaps of R_0, R_0C_0 and $R_0C_0C_0$ subcells by dashed curves. In the limit $x \to 0$, the three curves perfectly match with those of the main cell, C_0 and C_0C_0, respectively (solid curves).

Another exceptional case occurs in the gaps connected to the Dirac point of the magnetic Bloch band. In Fig. 4(b), we observe that the negative gaps of R_0 and C_0R_0 follow a curve slightly different from the rest in the limit of $x \to 0$. For R_0, the gap in the limit of $x \to 0$ leads to the point of $\phi = 1/2$ and $E = 0$ of the main diagram, where a pair of magnetic Bloch bands is touching just like in graphene due to the electron-hole symmetry of the Hofstadter model. Now the wavefunction of the Landau level n in graphene is composed of the φ_{n-1} and φ_n at different sublattices [70, 71], so that its length scale is just in the middle of those of $(n-1)$-th and n-th Landau levels in the conventional massive electron. Accordingly, the defect-localized states should have the intermediate localization length compared to the massive system. Indeed, the localization length of defect states in R_0 subcell for small x is given by $\xi \approx 1.98\, l_B$, which is between the values of $n = 1$ and 2 in Eq. (8). In Fig. 4(b), we see that C_0R_0 subcell also follows the same curves as R_0 subcell. This is because its negative principal gap leads to the point of $\phi = 1/4$ and $E = 0$, which is also the Dirac point.

D. The gradient of defect states and the magnetic moment

Generally, the in-gap defect states in a time-reversal-symmetry broken system are accompanied by an orbital current circulation [59, 72]. Here we find that the magnetic moment created by the orbital current of the defect states in our system is precisely related to the gradient of fractal defect states on the Hofstadter diagram. The local electric current J_{nm} from site m to site n is calculated by

$$J_{nm} = i\frac{(-e)t}{\hbar}(e^{i\theta_{mn}}\psi_n^*\psi_m - \text{c.c.}). \tag{9}$$

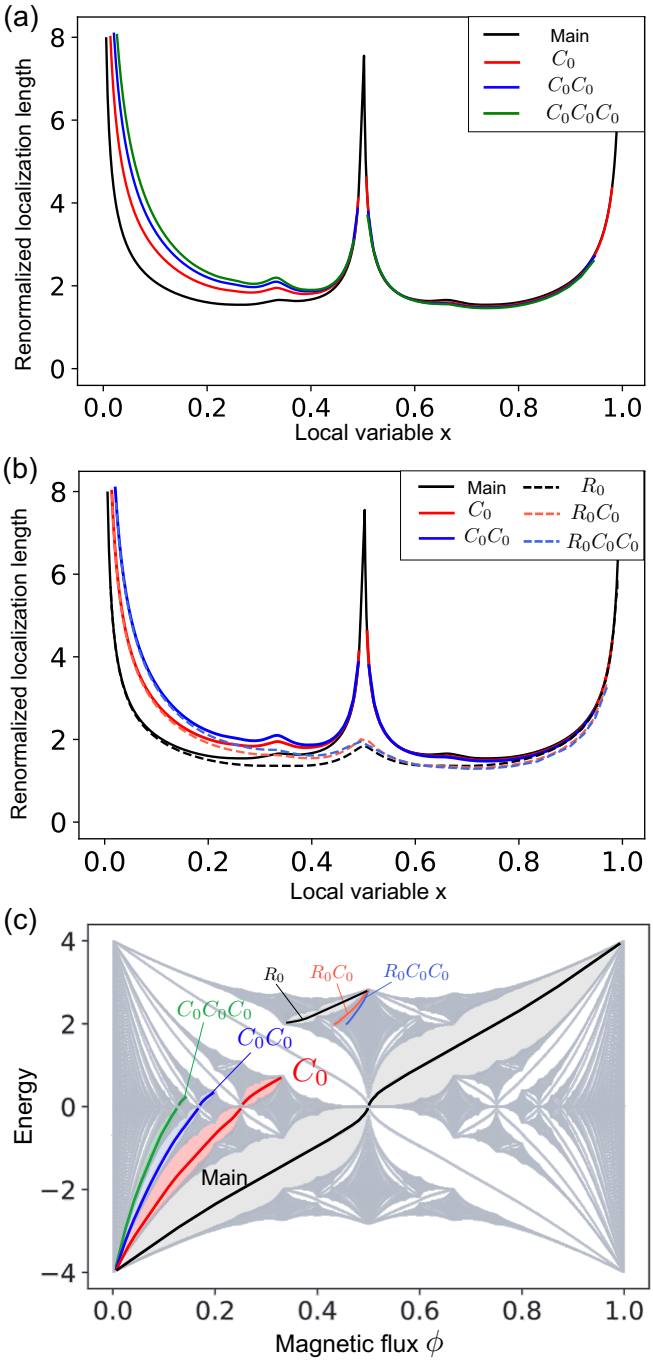

FIG. 5. (a) Renormalized localization lengths of the positive principal gaps of the main cell, C_0, C_0C_0 and $C_0C_0C_0$ subcells [ξ, $(\phi^{C_0}/x)\xi^{C_0}$, $(\phi^{C_0C_0}/x)\xi^{C_0C_0}$, $(\phi^{C_0C_0C_0}/x)\xi^{C_0C_0C_0}$, respectively] as functions of the local variable x. (b) The same plot as (a), with dashed lines indicating the renormalized localization lengths for R_0, R_0C_0 and $R_0C_0C_0$ subcells [$\phi^{R_0}\xi^{R_0}$, $(\phi^{R_0C_0}\phi^{C_0}/x)\xi^{R_0C_0}$, $(\phi^{R_0C_0C_0}\phi^{C_0C_0}/x)\xi^{R_0C_0C_0}$, respectively]. (c) The positive principal gaps of the main cell, C_0, C_0C_0 and $C_0C_0C_0$ subcells, which correspond to the first, second, third and forth Landau-level gaps in $\phi \to 0$, respectively. Similarly, the positive principal gaps of R_0C_0 and $R_0C_0C_0$ subcells correspond to the second and third Landau-level gaps, respectively, of the magnetic Bloch band in $\phi \to 1/2$.

The right column in Fig. 3 shows that the local current calculated for the defect states (i), (ii) and (iii).

The thickness of and the size of arrows are proportional to the absolute value of current.

Here the current rotates in the clockwise direction, i.e., it has a negative magnetic moment.

Actually, the direction of the current synchronizes with the gradient of the defect energy level in the Hofstadter diagram, because the orbital magnetic moment is given by $m = -dE/dB$ (see the Appendix C for the proof). In other words, a defect state in the Hofstadter butterfly precisely tunes its own current circulation, in such a way that the energy level stays inside the fractal gap in changing a magnetic field.

IV. MULTI-POINT VACANCIES

We also consider various multi-point vacancies in Fig. 6; (a) consecutive two-point defect, (b) two split defects and (c) three-point defect. The corresponding spectra of 30×30 superlattice are shown in Fig. 6, where we observe that the number of defect states in every single fractal gap matches that of the missing sites in the defect.

If we carefully look at the weak magnetic field regime in each case of Fig. 6, we observe that some defect states are absorbed into the bulk states in decreasing the magnetic field, and eventually only a single defect state is left in each gap in the limit of $B \to 0$. This is naturally expected in the continuum limit such that the magnetic length is much larger than the lattice constant. There the defect can be replaced by a single delta function regardless of its detailed internal structure, and it supports only a single impurity level [48].

By comparing Figs. 6(a) and (b), we notice that the two defect energy levels get closer as the distance between the two defect sites gets further away. This is a consequence of the hybridization of the defect states of two single vacancy sites, where the coupling strength exponentially decreases as the distance increases. A similar effect is also found in defect states in graphene [52]. We see the same tendency consistently in all the fractal gaps.

When we increase the number of missing atoms, the defect eventually becomes a big hole like the inner edge of the Corbino disk [73]. In the process, we expect that more and more defect levels fill in the energy gaps, and the orbital current of the defect states eventually becomes the chiral current of the quantum Hall edge channels. In that sense, the orbital current of our defect localized state can be viewed as a quantized version of the quantum Hall edge current in the atomic limit. Therefore the emergence of the defect levels in the fractal gaps may be viewed as a sort of the bulk-edge correspondence [74, 75] requiring the existence of the edge states in a bulk gap with a non-zero Chern number. However, it should also be noted that the number of the defect states in each gap is not at all related to the Chern number, but it just coincides with the number of missing sites for any gaps.

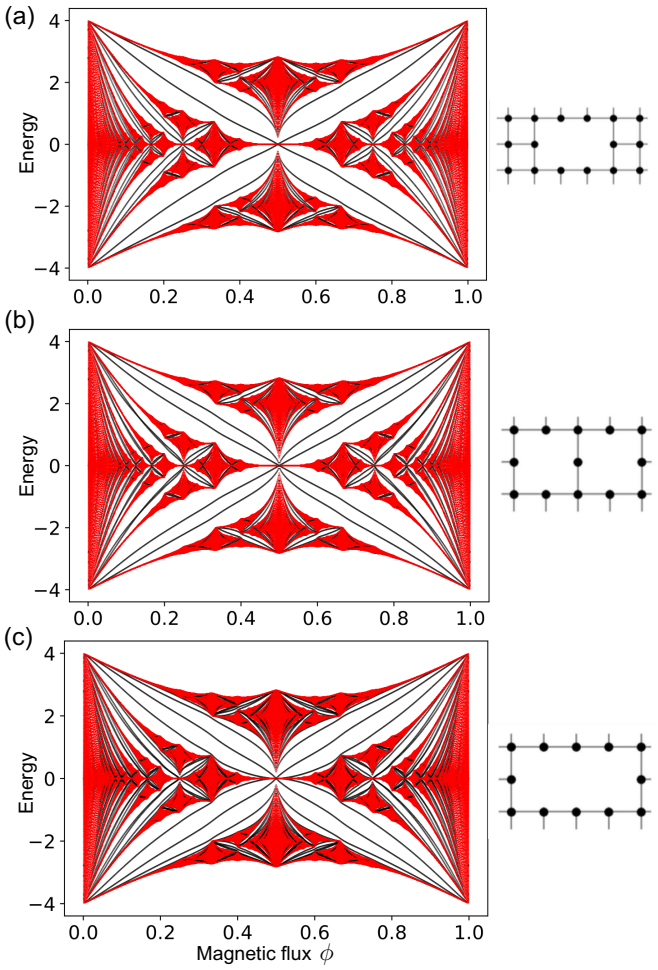

FIG. 6. Energy spectra of 30×30 superlattice with (a) consecutive two-point defect, (b) two split defects and (c) consecutive three-point defect.

V. CONCLUSION

We have reported that the defect-localized states fractally appear in every single band gap of the Hofstadter butterfly. Those states in different energy gaps have all different length scale in the spatial decay, while they follow a universal curve after the appropriate fractal scaling. Each defect state has its own characteristic magnetic moment, which is exactly linked to the gradient of the corresponding bulk energy gap in the Hofstadter diagram.

While the previous observations of Hofstadter butterfly have been mainly conducted by spectroscopic/transport measurements of the energy gap structure, our work provides a powerful method to observe the fractal nature in the wavefunction by measuring the spatial decay of the defect states using scanning tunneling spectroscopy.

ACKNOWLEDGMENTS

We thank Kin-ya Oda for fruitful discussions. This work was supported by Grant-in-Aid for JSPS Research Fellow, No. JP19J20559, JP19J11073, JSPS KAKENHI Grant Number JP20H01840 and JP20H00127 and by JST CREST Grant Number JPMJCR20T3, Japan.

Appendix A: Fractal Structure and Wavefunction on a honeycomb lattice with a defect

We consider defect-localized states on a honeycomb superlattice with a single-site defect (Fig. 7). We assume that the system is periodic with $N \times N$ supercell and every single supercell includes a single vacancy site. Now we take the super period $N = 20$, which is taken to be sufficiently large to avoid interference between defect-localized states in neighboring cells. The Bloch electron wavefunctions obey the magnetic Bloch condition:

$$\psi(\boldsymbol{r} + \boldsymbol{L}_1) = e^{ik_x L_1} e^{-i2\pi eBL_1 y} \psi(\boldsymbol{r}), \tag{A1}$$

$$\psi(\boldsymbol{r} + \boldsymbol{L}_2) = e^{ik_y L_2} \psi(\boldsymbol{r}), \tag{A2}$$

where $\boldsymbol{L}_1 = (\sqrt{3}Na/2, 0)$ and $\boldsymbol{L}_2 = (0, Na)$ are the primitive lattice vectors of the magnetic unit cell.

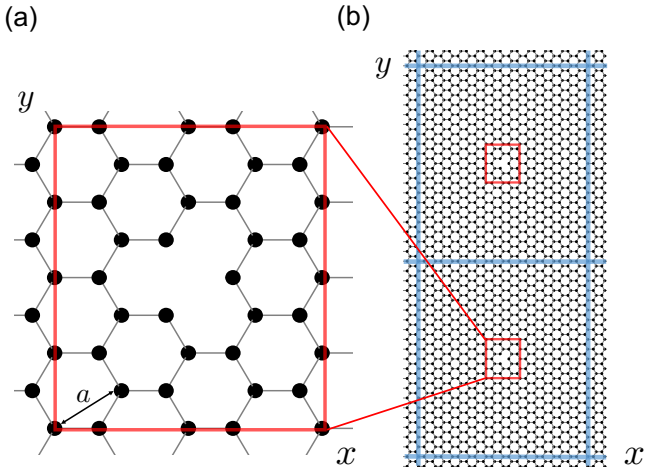

FIG. 7. Honeycomb lattice with a single point vacancy and (b) its periodic superlattice with 20×20 supercel

Fig. 8(a) shows the energy spectrum of 20×20 superlattice in a honeycomb lattice with a single defect, plotted against the magnetic flux ϕ. The red and black dots represent the bulk states and the defect-localized states, respectively. Here the defect-localized states are identified by the condition that the wave amplitude within $2\sqrt{3}a$ from the defect point is more than 50% of the total amplitude. We observe that a defect level exists in every single gap, indicating that the spectrum of the defect states inherits the nested fractal structure of the Hofstadter butterfly, same as the square lattice case.

To compare uniformly the localization lengths in different fractal generation gaps, we again define the subcell decomposition and the local variable y in a honeycomb lattice. As shown in Fig. 8(b), the main energy spectrum in $0 \le \phi \le 1$ includes the self-similar structure subcell H_n $(n = 0, \pm 1, \cdots)$. In fact, the gap structure of each subcell plotted against the local variable y $(0 \le y \le 1)$ is identical to that of the main spectrum plotted against the magnetic flux ϕ $(0 \le \phi \le 1)$. The relationship between the global variable ϕ and local variable y is

$$\phi^{H_n}(y) = (n + y + 2)^{-1}. \tag{A3}$$

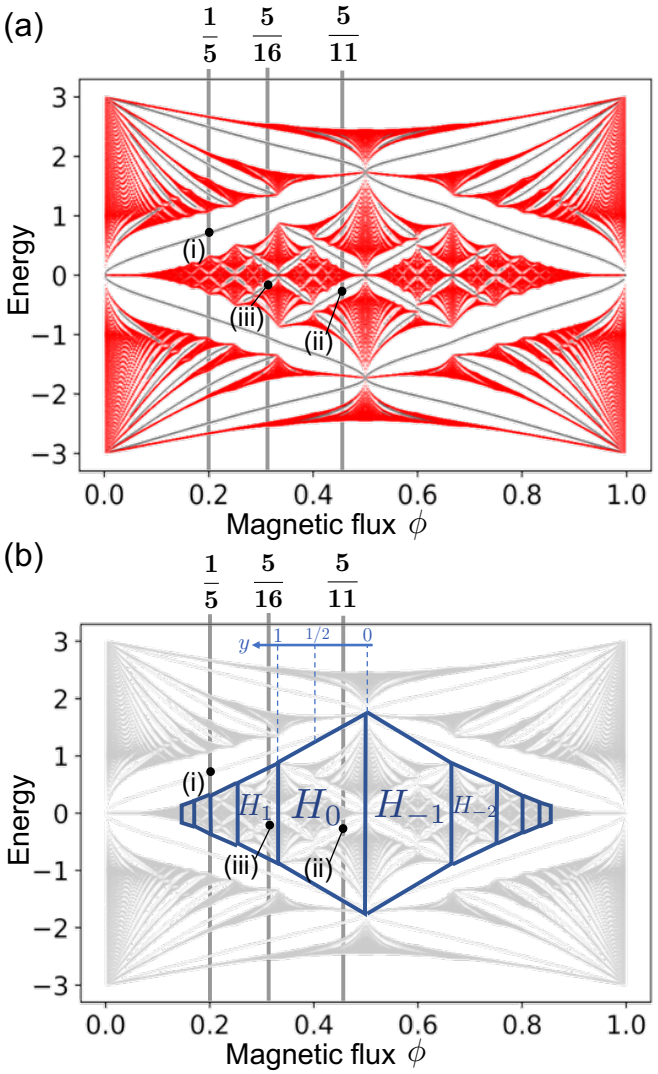

FIG. 8. (a) Energy spectrum of 20×20 honeycomb superlattice with a single-site defect, which is plotted against the magnetic flux ϕ. The red and black dots represent the bulks states and the defect-localized states, respectively. The labels (i), (ii) and (iii) correspond to the wavefunctions shown in Fig. 9. (b) Subcell decomposition of the Hofstadter butterfly in a honeycomb lattice. The states (i), (ii) and (iii) belong to the positive gradient principal gaps of the main spectrum, H_0 and H_1 subcells, respectively.

In the main spectrum, the global variable ϕ corresponds to the local variable y since the main spectrum can be viewed as a single subcell. In the following, we show the amplitude and the electric current of the corresponding defects states of different subcells at the same local variable y.

The left panels in Fig. 9 show the distribution of the wave amplitude of three defect levels (i), (ii) and (iii) indicated in Fig. 8, which are taken from the positive principal gaps of the main spectrum, H_0 and H_1 subcells, respectively, with the same local variable $y = 1/5$. From the equation (A3), the global variables ϕ for (i), (ii) and (iii) are $1/5$, $\phi^{H_0}(1/5) = 5/11$ and $\phi^{H_1}(1/5) = 5/16$, respectively. We can observe that the defect wavefunctions localize around the defect with different length scales.

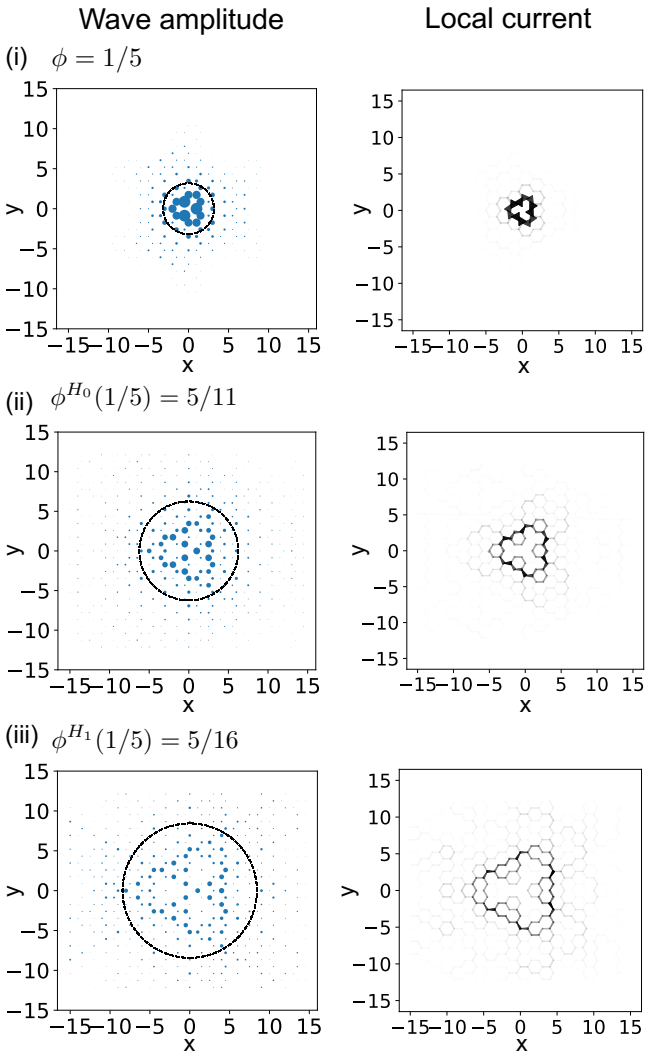

FIG. 9. Distribution of the wave amplitude (left) and the local electric current (right) of the defect states (i), (ii) and (iii), which are indicated in Fig. 8. The dots size in the left figures represents the magnitude of wavefunction, and thickness and color depth of the arrows in the right figures represent the local current amplitude.

Moreover, the right panels in Fig. 9 represent that the local current calculated for the defect states (i), (ii) and (iii). As discussed above, the magnetic moment created by the local current coincides with the gradient on the Hofstadter diagram (Fig. 8). Actually, the currents rotate in the clockwise direction, and their direction synchronizes with the gradient of the defect energy levels in the Hofstadter diagram. The same properties as the square lattice case (the localization around the defect, the fractality of localization length, and the correspondence between magnetic moment and gradient of defect states) are observed in a honeycomb lattice case.

Appendix B: Analytical expression of the localization length in the continuum model

Here we analytically derive the localization length of the defect localized state using the continuum model [76], and compare it to our numerical results for the lattice model. We consider a two-dimensional continuum Hamiltonian with a delta-impurity potential which corresponds to a point defect in the lattice model,

$$H = -\frac{1}{2}(\boldsymbol{\nabla} - ie\boldsymbol{A})^2 + \lambda\delta^2(\boldsymbol{x}) \quad (m = \hbar = c = 1), \quad \text{(B1)}$$

where λ represents the amplitude of the impurity potential. Using Green function method following [76], the wavefunction of impurity-localized state between the Landau level $n-1$ and n is given by

$$\varphi_{\mathrm{imp},n}(\boldsymbol{x}) = \sqrt{\frac{eB}{2\pi\psi'(-k_n)}}M(\boldsymbol{x},0)e^{-eB\boldsymbol{x}^2/4} \times \sum_{m=0}^{\infty}\frac{L_m(eB\boldsymbol{x}^2/2)}{k_n - m}, \quad \text{(B2)}$$

where ψ' represents a trigamma function, $M(\boldsymbol{x},\boldsymbol{x}') = \exp[ie\int_{\boldsymbol{x}'}^{\boldsymbol{x}}\boldsymbol{A}\cdot d\boldsymbol{\ell}]$, L_m is the Laguerre polynomial. The k_n $(n-1 < k_n < n)$ is determined by

$$\psi(-k_n) - \frac{2\pi}{\lambda_R} = 0, \quad \text{(B3)}$$

where ψ is a digamma function, and λ_R is a renormalized parameter determined by

$$\frac{1}{\lambda_R} = \frac{1}{\lambda} - \frac{1}{2\pi}(\gamma + \ln\alpha). \quad \text{(B4)}$$

Hhere $\gamma \approx 0.5772$ is Euler's constant, and α is an exponent of the convergence factor $e^{-\alpha n}$ in the sum over Landau level index n.

Finally, the localization length of the impurity-localized state can be estimated as

$$\xi_n \equiv \left[\int d^2\boldsymbol{x}\varphi^*_{\mathrm{imp},n}|\boldsymbol{x}|^2\varphi_{\mathrm{imp},n}\right]^{1/2} = 2\sqrt{k_n + 1/2 + [\psi'(-k_n)]^{-1}}\,\ell_B. \quad \text{(B5)}$$

In the derivation, we used the identity

$$\int_0^\infty dt\, te^{-t} \sum_{m,m'} \frac{L_m(t)L_{m'}(t)}{(k_n-m)(k_n-m')} = (2k_n+1)\psi'(-k_n)+2, \quad \text{(B6)}$$

which is derived by the generating function of Laguerre polynomial

$$U(t,s) = \frac{\exp(-t\frac{s}{1-s})}{1-s} = \sum_{m=0}^{\infty} L_m(t)s^m. \quad \text{(B7)}$$

In what follows, we roughly evaluate the parameters λ and α for the square lattice tight-binding model. The potential amplitude λ is estimated as $\lambda \sim tm^*a^2/\hbar^2$ by the dimensional analysis (here we restored the dimension), where m^* is the electron effective mass. Since we have $m^* = \hbar^2/(2ta^2)$ for the bottom of the cosine band, λ is the order of 1. As the convergence factor α should be the inverse of the maximum Landau level index, n_c. The n_c is roughly estimated as $(n_c+1/2)\hbar eB/m^* \sim E_c$ where $E_c \sim 4t$ is the band width as the cut-off energy. Then we have $\alpha \sim 1/n_c \sim \hbar eB/(4m^*t) = \pi\phi$, where $\phi = Ba^2/(h/e)$ is the magnetic flux per a unit cell. From the above estimation and Eq. (B3), we find $k_n \approx n-1$ and $[\psi'(-k_n)]^{-1} \ll 1$ for the low magnetic field regime $\phi \ll 1$, and then (B5) becomes

$$\xi_n \approx 2\sqrt{n-1/2}\,\ell_B. \quad \text{(B8)}$$

Although the estimation of the parameters is rather crude, it nicely agrees with the numerical result (8).

Appendix C: The gradient of defect states and the magnetic moment

We prove that the gradient of a defect energy level in the Hofstadter diagram coincides with the magnetic moment created by the local electric current. For this purpose we show that the magnetic moment $\boldsymbol{m}$ obeys Eq. (C9) in the presence of a generic potential $V(\boldsymbol{r})$ in quantum mechanics. We consider the system described by the Hamiltonian,

$$H_0 = \frac{1}{2m}(-i\boldsymbol{\nabla} + e\boldsymbol{A})^2 + V(\boldsymbol{r}) \quad (\hbar = 1). \quad \text{(C1)}$$

Considering a small change in the magnetic field, we obtain the perturbed Hamiltonian

$$H = \frac{1}{2m}(-i\boldsymbol{\nabla} + e(\boldsymbol{A}+\delta\boldsymbol{A}))^2 + V(\boldsymbol{r}) \quad \text{(C2)}$$

$$= H_0 - \frac{1}{2}(\boldsymbol{J}\cdot\delta\boldsymbol{A} + \delta\boldsymbol{A}\cdot\boldsymbol{J}) \equiv H_0 + \delta H, \quad \text{(C3)}$$

where $\boldsymbol{J}$ is the current operator

$$\boldsymbol{J} = (-e)i[\boldsymbol{r}, H_0] = (-e)\frac{-i\boldsymbol{\nabla} + e\boldsymbol{A}}{m}. \quad \text{(C4)}$$

The variation of the energy δE within the first order perturbation is

$$\delta E = \langle\psi_0|\,\delta H\,|\psi_0\rangle = -\frac{1}{2}\langle\psi_0|\,(\boldsymbol{J}\cdot\delta\boldsymbol{A}+\delta\boldsymbol{A}\cdot\boldsymbol{J})\,|\psi_0\rangle\,, \quad \text{(C5)}$$

where ψ_0 is the eigenfunction of H_0. The first term in the most right hand side in (C5) is evaluated as follows:

$$\langle\psi_0|\,(\boldsymbol{J}\cdot\delta\boldsymbol{A})\,|\psi_0\rangle = \int d\boldsymbol{r}d\boldsymbol{r}'\psi_0^*(\boldsymbol{r})\boldsymbol{J}(\boldsymbol{r})\delta(\boldsymbol{r}-\boldsymbol{r}')\psi_0(\boldsymbol{r})\cdot\delta\boldsymbol{A}(\boldsymbol{r}'). \quad \text{(C6)}$$

We can evaluate the second term in a similar way, and finally obtain

$$\delta E = \int d\boldsymbol{r}'\boldsymbol{j}(\boldsymbol{r}')\cdot\delta\boldsymbol{A}(\boldsymbol{r}'). \quad \text{(C7)}$$

Here we used the local current operator $\boldsymbol{j}$,

$$\boldsymbol{j}(\boldsymbol{r}') \equiv -\frac{1}{2}\int d\boldsymbol{r}\psi_0^*(\boldsymbol{r})(\boldsymbol{J}(\boldsymbol{r})\delta(\boldsymbol{r}-\boldsymbol{r}')+\delta(\boldsymbol{r}-\boldsymbol{r}')\boldsymbol{J}(\boldsymbol{r}))\psi_0(\boldsymbol{r}). \quad \text{(C8)}$$

By using the expression of the magnetizing current $\boldsymbol{j} = \boldsymbol{\nabla}\times\boldsymbol{m}$, one can find that the magnetic moment $\boldsymbol{m}$ obeys

$$\boldsymbol{m} = -\frac{dE}{d\boldsymbol{B}}. \quad \text{(C9)}$$

[1] P. G. Harper, Proceedings of the Physical Society. Section A **68**, 879 (1955).
[2] P. G. Harper, Proceedings of the Physical Society. Section A **68**, 874 (1955).
[3] J. Zak, Phys. Rev. **134**, A1602 (1964).
[4] M. Y. Azbel, Zh. Eksp. Teor. Fiz. **46**, 929 (1964).
[5] D. R. Hofstadter, Phys. Rev. B **14**, 2239 (1976).
[6] G. H. Wannier, physica status solidi (b) **88**, 757 (1978).
[7] G. H. Wannier, G. M. Obermair, and R. Ray, physica status solidi (b) **93**, 337 (1979).
[8] F. H. Claro and G. H. Wannier, Phys. Rev. B **19**, 6068 (1979).
[9] R. Rammal, J. Phys. France **46**, 1345 (1985).
[10] D. Pfannkuche and R. R. Gerhardts, Phys. Rev. B **46**, 12606 (1992).
[11] G. Gumbs, D. Miessein, and D. Huang, Phys. Rev. B

52, 14755 (1995).
[12] M. Koshino, H. Aoki, K. Kuroki, S. Kagoshima, and T. Osada, Phys. Rev. Lett. **86**, 1062 (2001).
[13] Y. Xiao, V. Pelletier, P. M. Chaikin, and D. A. Huse, Phys. Rev. B **67**, 104505 (2003).
[14] J. Herzog-Arbeitman, Z.-D. Song, N. Regnault, and B. A. Bernevig, Phys. Rev. Lett. **125**, 236804 (2020).
[15] G. Gumbs, A. Iurov, D. Huang, and L. Zhemchuzhna, Phys. Rev. B **89**, 241407 (2014).
[16] T. Bilitewski and N. R. Cooper, Phys. Rev. A **91**, 063611 (2015).
[17] T. Qin and W. Hofstetter, Phys. Rev. B **96**, 075134 (2017).
[18] S. H. Kooi, A. Quelle, W. Beugeling, and C. Morais Smith, Phys. Rev. B **98**, 115124 (2018).
[19] L. Du, Q. Chen, A. D. Barr, A. R. Barr, and G. A. Fiete, Phys. Rev. B **98**, 245145 (2018).
[20] S. Owerre, Annals of Physics **399**, 93 (2018).
[21] Y.-Z. Chou, F. Wu, and S. Das Sarma, Phys. Rev. Research **2**, 033271 (2020).
[22] B. Dey and T. K. Ghosh, Phys. Rev. B **99**, 205429 (2019).
[23] J. Bellissard, Operator Algebras and Application, edited by D. E. Evans and M. Takesaki (Cambridge University Press, Cambridge, England, 1988), Vol. 2.
[24] B. Helffer and J. Sjöstrand, Suppl. Bull. Soc. Math. France **116(4)**, 34 (1988).
[25] Y. Last, Commun.Math. Phys. **164**, 421 (1994).
[26] E. Prodan, Phys. Rev. B **91**, 245104 (2015).
[27] K. Ikeda, Journal of Mathematical Physics **59**, 061704 (2018).
[28] K. Ikeda, Annals Phys. **397**, 136 (2018).
[29] K. Ikeda, (2018), arXiv:1812.11879 [cond-mat.mes-hall].
[30] Y. Hatsuda, H. Katsura, and Y. Tachikawa, New J. Phys. **18**, 103023 (2016), arXiv:1606.01894 [hep-th].
[31] Z. Duan, J. Gu, Y. Hatsuda, and T. Sulejmanpasic, ArXiv e-prints (2018), arXiv:1806.11092 [hep-th].
[32] T. Schlösser, K. Ensslin, J. P. Kotthaus, and M. Holland, Semiconductor Science and Technology **11** (1996).
[33] C. Albrecht, J. H. Smet, K. von Klitzing, D. Weiss, V. Umansky, and H. Schweizer, Phys. Rev. Lett. **86**, 147 (2001).
[34] M. Geisler, J. Smet, V. Umansky, K. Von Klitzing, B. Naundorf, R. Ketzmerick, and H. Schweizer, Phys. Rev. Lett. **92**, 256801 (2004).
[35] D. Jaksch and P. Zoller, New Journal of Physics **5**, 56 (2003).
[36] M. Aidelsburger, M. Atala, M. Lohse, J. T. Barreiro, B. Paredes, and I. Bloch, Phys. Rev. Lett. **111**, 185301 (2013).
[37] H. Miyake, G. A. Siviloglou, C. J. Kennedy, W. C. Burton, and W. Ketterle, Phys. Rev. Lett. **111**, 185302 (2013).
[38] C. R. Dean, L. Wang, P. Maher, C. Forsythe, F. Ghahari, Y. Gao, J. Katoch, M. Ishigami, P. Moon, M. Koshino, T. Taniguchi, K. Watanabe, K. L. Shepard, J. Hone, and P. Kim, Nature **497**, 598 (2013).
[39] B. Hunt, J. D. Sanchez-Yamagishi, A. F. Young, M. Yankowitz, B. J. LeRoy, K. Watanabe, T. Taniguchi, P. Moon, M. Koshino, P. Jarillo-Herrero, and R. C. Ashoori, Science **340** (2013), 10.1126/science.1237240.
[40] L. A. Ponomarenko, R. V. Gorbachev, G. L. Yu, D. C. Elias, R. Jalil, A. A. Patel, A. Mishchenko, A. S. Mayorov, C. R. Woods, J. R. Wallbank, M. Mucha-Kruczynski, B. A. Piot, M. Potemski, I. V. Grigorieva, K. S. Novoselov, F. Guinea, V. I. Falko, and A. K. Geim, Nature **497**, 594 (2013).
[41] P. Roushan, C. Neill, J. Tangpanitanon, V. M. Bastidas, A. Megrant, R. Barends, Y. Chen, Z. Chen, B. Chiaro, A. Dunsworth, A. Fowler, B. Foxen, M. Giustina, E. Jeffrey, J. Kelly, E. Lucero, J. Mutus, M. Neeley, C. Quintana, D. Sank, A. Vainsencher, J. Wenner, T. White, H. Neven, D. G. Angelakis, and J. Martinis, Science **358**, 1175 (2017).
[42] U. Kuhl and H.-J. Stöckmann, Phys. Rev. Lett. **80**, 3232 (1998).
[43] O. Richoux and V. Pagneux, Europhysics Letters (EPL) **59**, 34 (2002).
[44] X. Ni, K. Chen, M. Weiner, D. J. Apigo, C. Prodan, A. Alù, E. Prodan, and A. B. Khanikaev, Commun Phys **2**, 256 (2019).
[45] T. Ando and Y. Uemura, Journal of the Physical Society of Japan **36**, 959 (1974).
[46] T. Ando, Journal of the Physical Society of Japan **37**, 622 (1974).
[47] T. Ando, Y. Matsumoto, and Y. Uemura, Journal of the Physical Society of Japan **39**, 279 (1975).
[48] R. E. Prange, Phys. Rev. B **23**, 4802 (1981).
[49] R. Joynt and R. E. Prange, Phys. Rev. B **29**, 3303 (1984).
[50] S. Gredeskul, M. Zusman, Y. Avishai, and M. Azbel', Physics Reports **288**, 223 (1997).
[51] Y. Niimi, H. Kambara, T. Matsui, D. Yoshioka, and H. Fukuyama, Phys. Rev. Lett. **97**, 236804 (2006).
[52] A. L. C. Pereira and P. A. Schulz, Phys. Rev. B **78**, 125402 (2008).
[53] S. İslamoğlu, M. O. Oktel, and O. Gülseren, Journal of Physics: Condensed Matter **24**, 345501 (2012).
[54] S. İslamoğlu, M. O. Oktel, and O. b. u. Gülseren, Phys. Rev. B **85**, 235414 (2012).
[55] J. G. Pedersen and T. G. Pedersen, Phys. Rev. B **87**, 235404 (2013).
[56] C. Zhou, M. Berciu, and R. N. Bhatt, Phys. Rev. B **71**, 125310 (2005).
[57] E. N. Grishanov and I. Y. Popov, Russ. J. Math. Phys. **25**, 277 (2018).
[58] Y. Matsuki and K. Ikeda, Journal of Physics Communications **3**, 055003 (2019).
[59] S.-S. Diop, L. Fritz, M. Vojta, and S. Rachel, Phys. Rev. B **101**, 245132 (2020).
[60] R. Peierls, Zeitschrift für Physik **80**, 763 (1933).
[61] D. Xiao, M.-C. Chang, and Q. Niu, Rev. Mod. Phys. **82**, 1959 (2010).
[62] P. Moon and M. Koshino, Phys. Rev. B **85**, 195458 (2012).
[63] G. G. Naumis and J. L. Aragón, Phys. Rev. B **54**, 15079 (1996).
[64] G. G. Naumis, Phys. Rev. B **59**, 11315 (1999).
[65] G. G. Naumis, Physics Letters A **309** (2003), https://doi.org/10.1016/S0375-9601(03)00247-0.
[66] A. H. MacDonald, Phys. Rev. B **28**, 6713 (1983).
[67] J.-W. Rhim and K. Park, Phys. Rev. B **86**, 235411 (2012).
[68] N. Yoshioka, H. Matsuura, and M. Ogata, Journal of the Physical Society of Japan **85**, 064712 (2016), https://doi.org/10.7566/JPSJ.85.064712.
[69] A. Mishra, S. R. Hassan, and R. Shankar, Phys. Rev. B **95**, 035140 (2017).
[70] N. H. Shon and T. Ando, Journal of the Physical Society

of Japan **67**, 2421 (1998).
[71] Y. Zheng and T. Ando, Phys. Rev. B **65**, 245420 (2002).
[72] V. B. Jha, G. Rani, and R. Ganesh, Phys. Rev. B **95**, 115434 (2017).
[73] M. E. Cage, K. Klitzing, A. Chang, F. Duncan, M. Haldane, R. Laughlin, A. Pruisken, and D. Thouless, The quantum Hall effect (Springer Science & Business Media, 2012).
[74] Y. Hatsugai, Phys. Rev. Lett. **71**, 3697 (1993).
[75] Y. Hatsugai, Phys. Rev. B **48**, 11851 (1993).
[76] R. M. Cavalcanti and C. A. A. de Carvalho, Journal of Physics A: Mathematical and General **31**, 2391 (1998).